A functional modelling approach for reconstructing 3 and 4 dimensional wet refractivity fields in the lower atmosphere using GNSS measurements

Ehsan Forootan[1], Masood Dehvari[2], Saeed Farzaneh[2*], Ali Sam Khaniani[3]

[1] Geodesy and Earth Observation Group, Department of Planning, Aalborg University, Rendsburggade 14, 9000, Aalborg, Denmark

[2] School of Surveying and Geospatial Engineering, College of Engineering, University of Tehran, North Kargar Street, Central Building of the College of Engineering, 1439957131 Tehran, Iran

[3] Babol Noshirvani University of Technology, Civil Engineering Department, P.O. Box 484, Shariati Ave., Babol, Mazandaran 47148-71167, Iran

* Correspondence: farzaneh@ut.ac.ir; Tel.: +986114528 (Iran)

Abstract

The GNSS tomography provides the opportunity to estimate atmospheric wet refractivity, which is important for precise positioning and navigation, as well as for constraining weather and climate models. The GNSS-derived water vapor is often estimated by implementing voxel-based inversions, but this technique is numerically unstable due to the high number of unknown parameters especially in networks covering large areas or when the spatial resolution increases. To mitigate this problem, in this study, we introduce functional based 3 and 4 dimensional (3D and 4D) inversions. Here, the horizontal changes are modelled by the spherical cap harmonic functions. For the vertical component, empirical orthogonal functions derived from ERA5 (Empirical Reanalysis Fifth generation) are applied as background model. The time-dependency is accounted for by applying polynomial spline functions. Numerical results are based on a network of about 190 GPS stations in Germany during 15 days in summer and winter of 2018. Observations from 8 radiosonde stations are applied for comparisons. Our results indicate that the functional tomography is effective and retrieves wet refractivity indices with the mean RMSE (Root Mean Square Error) of about 1.9 ppm. These values are found to be up to 22% smaller than those derived by comparing ERA5 with the radiosonde data.

Keywords: Water Vapor; GNSS; Functional-based Tomography; 3D and 4D model

1. Introduction

Water vapor or wet refractivity index in the atmosphere is one of the most substantial parameters for weather forecasting models, and its temporal and spatial changes can be an indicator of climate change. Today, using assimilation of various satellite and in-situ observations of different spatial and temporal resolutions, analysis and reanalysis weather products are being generated. Global Circulation Models (GCMs) reproduce both the large-scale and mesoscale patterns of atmospheric circulations in which water vapor can be considered as one of their valuable outputs. As the resolution of numerical models increases in both temporal and spatial scale, more detailed atmospheric products are available. The European Center for Medium Range Weather Forecast (ECMWF) provides global forecasts, analysis and re-analysis at different spatial resolutions, e.g., 0.08° × 0.08°. The state-of-the-

art of global scale products may however be insufficient to represent small-scale and terrain-driven meteorological features (Carvalho et al. , 2014).

In order to present the state of the atmosphere in a smaller scale and to consider specific dynamical processes, regional numerical models, such as the Weather Research and Forecasting Model (WRF) are utilized (Skamarock et al. , 2008; Lian et al. , 2018). For producing more realistic estimates, these models are needed to be constrained by observations as shown by, e.g., Leontiev et al. (2021).

Different observation tools are available to measure wet refractivity indices such as the radiosonde stations, satellite-based microwave interferometry, radiometer on-board satellites, radio occultation, and the ground-based Global Navigation Satellite System (GNSS) stations (see a review in Guerova et al. , 2016). The heterogeneous distribution of water vapor, its drastic spatial and temporal changes, as well as the resolution limitations of satellite-based observations and radiosonde stations data are among the main challenges for accurate representation of this variable (see more details in, e.g., Bevis et al. , 1992).

By emerging the GNSS technology a new opportunity has been opened for atmospheric investigations such as precipitation and rainfall prediction, global and local climate change studies, and natural hazard prediction (Stierman, 2017). Particularly, the ground based GNSS stations are built in many regions to facilitate accurate positioning and navigation, where their measurements can also be used for estimating water vapor with high temporal resolution. Generally speaking, the atmosphere causes delay on GNSS that are predominantly known as the ionosphere and troposphere effects (Hofmann-Wellenhof et al. , 2007). By analyzing GNSS networks, the tropospheric wet delay can be estimated and used for assessing water vapor or its equivalent wet refractivity indices (Subirana et al. , 2013).

From GNSS constellations, most of the existing studies utilize observations by the US's Global Positioning System (GPS) to estimate water vapor in the atmosphere since it is the oldest constellation with relatively stable number of satellites in the view of ground based stations. For example, Bevis et al. (1992) applied GPS measurements to estimate the Perceptible Water Vapor (PWV) and showed that they are in agreement with the radiosonde data with an accuracy of 1-2 millimeter. For the study of climate changes, Alshawaf et al. (2017) estimated changes between -1.5 and 2 mm/decade in PWV trends for time series about 10 to 19 years using GNSS observation over Germany. Li et al. (2015) used multi-GNSS observations for estimating real-time Integrated Water Vapor (IWV) and showed that the accuracy of estimates are increased to about 1.5 mm as a result of using the higher number of observations from multi-constellations compared with using only one of them.

In order to quantify water vapor, i.e., its spatial and temporal distribution in the atmosphere, the tomography method is introduced in previous studies (e.g., Ding et al., 2017, Flores et al., 2000, Nilsson and Gradinarsky, 2006, Xia et al., 2013). This is often implemented by estimating the wet refractive index from a GNSS network (Bosy et al. , 2010) using voxel-based approaches that formulate delays between GNSS satellites and receivers based on the direction and length of signals passing through each voxel box (Flores et al., 2000, Hirahara, 2000). However, the voxel-based formulation is an ill-posed inversion problem caused by the heterogeneous station's distribution within the network and the parallelism of some observational signals. As a result, some voxels remain empty and the GNSS signals do not pass through them (Bender and Raabe, 2007). Another problem is that the coefficients need

to be estimated for each voxel are highly correlated so that in general the equation system is not stable to be solved using an ordinary least squares optimization. Therefore, the estimation of tomographic unknown parameters using direct and iterative regularization methods has been under investigation since many years (Adavi and Mashhadi-Hossainali, 2015, Chen and Liu, 2014, Hirahara, 2000). The iterative regularization methods is often used in tomography problems. Because they do not need matrix inversion procedure and the optimum solution is obtained by iterative algorithms (Bender et al., 2011), where example include: the Algebraic Reconstruction Technique (ART) (Eggermont et al., 1981), the Simultaneous Iterative Reconstruction Technique (SIRT) (Trampert and Leveque, 1990), and the Multiplicative Iterative Reconstruction Technique (MART, Raymund et al., 1993). The advantage of these methods is the simplicity of calculations and the small amount of memory for implementation.

To improve on the distribution of GNSS measurements within a simulated voxel based inversion (employing iterative regularization methods), Wang et al. (2014) applied the measurements of BeiDou constellation and compared them that with GPS only observations. They obtained the Root Mean Square (RMS) of about 4 ppm for estimating wet refractivity indices in joint observation method. Xiaoying et al. (2014) used Gaussian constraints in the iterative regularization methods to account for voxels that are not passed by slants, and they showed that the accuracy of estimation can be improved. However, the iterative regularization methods have limitations such as their dependency on initial values and their sensitivity to the noise level of measurements. Besides, direct regularization methods require large amounts of memory due to the inverse matrix processing and matrix decomposition, which limits their application for dense tomography purposes.

An alternative approach to stabilize the voxel-based inversion can be realized by applying functional-based representations that considerably reduce the number of unknown parameters to be estimated for the modelling. The basic idea of this approach is to expand the spatial and temporal changes using basis functions that are often mutually orthogonal (to ease the computational procedure). This view has often been implemented in the area of ionosphere tomography using GNSS measurements (for details see e.g., Al-Fanek, 2013, Alizadeh, 2013, Farzaneh and Forootan, 2018, Limberger, 2015, Liu, 2004, Liu et al., 2011, 2014).

The aim of this study is to demonstrate the ability of 3D and 4D functional-based tomography formulations in retrieving the wet refractivity indices. To demonstrate the results, the horizontal (dimensions 1 and 2) changes are represented by the spherical cap basis functions, while the vertical changes (the 3rd dimension) are accounted for by introducing Empirical Orthogonal Functions (EOFs) from the wet refractivity fields of the latest ECMWF (European Centre for Medium-Range Weather Forecasts) reanalysis numerical model, i.e., ERA5 (Hersbach et al., 2020). The polynomial Spline basis functions are then used for modelling the time-dependent distribution of wet refractivity in the region of interest (the 4th dimension). Our motivation in selecting the spherical caps is due to their popularity (Liu, Chen, 2014, Liu, Chen, 2011, Razin and Voosoghi, 2017) and their simple computational requirements. The presented approach is however formulated in a generic form that other basis functions such as the Slepian functions (Farzaneh and Forootan, 2018) and 2D B-Splines (Limberger, 2015) can be replaced. The reliability of ERA5 for water vapor

estimation is shown, e.g., in (Yang et al. , 2019) and (Hu and Mallorquí, 2019). The numerical evaluations are performed over a network of about 190 GPS stations in Germany. The tomography time was also selected on days between January 13th till 2nd February 2018, and July 4th till 18th July 2018, at 12 and 24 UTC (Coordinated Universal Time). Data from eight radiosonde stations on the network have been used to evaluate the tomography results.

2. Methodology

2.1. Voxel-based tomography

Atmospheric tomography is referred to reconstructing parameters that have an effect on the GNSS signals passing through the atmosphere (Aster et al. , 2005). In the voxel-based formulation, the Slant Wet Delay (SWD) of GNSS is used as input, where the area of study is divided into voxels covering the area between surface of the Earth and satellites. Then a design matrix is built by calculating the length of arrays that pass through these voxels. Afterward, an inverse problem needs to be solved, from which the wet refractive index within the region of interest can be determined (Adavi and Mashhadi-Hossainali, 2014).

Here, we present the SWD estimation from the Global Positioning System (GPS) constellation. This can be extended to all GNSS constellations as shown by (Dong and Jin, 2018). The GPS slant wet delay measurements can be written as (Bevis, Businger, 1992):

$$SWD = 10^{-6} \int_{L} N_W \, dl \tag{1}$$

Where SWD represents the tropospheric slant wet delay, L is the signal length, and N_W is the wet term of refractivity. Assuming that the refractive index is constant in each voxel, Eq. (1) for wet tropospheric delay can be written in a discrete form (Bender et al. , 2013):

$$\mathrm{SWD} = \sum\nolimits_{i,j,k} N_{i,j,k} \, D_{i,j,k} \tag{2}$$

Where the subscripts i, j and k indicate the voxel position, $N_{i,j,k}$ are the wet tropospheric delay, and $D_{i,j,k}$ is the signal length passing through the specified voxel. Providing all the wet tropospheric delay measurements, the observation equation is:

$$\mathbf{Y} = \mathbf{A}\,\mathbf{N} \tag{3}$$

Where $\mathbf{Y}$ is the vector of wet tropospheric delay measurements, $\mathbf{A}$ is the tomographic design matrix, and $\mathbf{N}$ is vector of unknown parameters (i.e., wet refractivity values).

2.2. Spherical Cap Harmonics

The wet refractivity expression using the spherical harmonics expansion can be written as:

$$N_i(\lambda, \theta) = \sum_{n=0}^{k} \sum_{m=0}^{n} [a_n^m \cos(m\lambda) + b_n^m \sin(m\lambda)] \, P_n^m(\cos\theta) \tag{4}$$

Where N_i is the 2D wet refractivity, a_n^m and b_n^m are the coefficients of spherical harmonics expansion, λ and θ are the geographic longitudes and colatitudes, and $P_n^m(\cos\theta)$ is the normalized Legendre function of order m and degree n. If the region of study is part of a sphere, the spherical harmonics are not the most appropriate basis for the expansion because the Legendre functions lose their orthogonality (Haines, 1985). To overcome this problem, the spherical cap harmonics has been proposed with the Legendre functions whose derivatives are zero at the corners of the cap-shaped region with a half-angle θ_0, see details in (Haines, 1985).

Boundary conditions for implementing spherical cap harmonics can be written as follows (Haines, 1985):

$$\frac{dP_{n_k}^m(cos\theta_0)}{d\theta} = 0 \qquad \text{for } k - m = \text{even} \tag{5}$$

$$P_{n_k}^m(cos\theta_0) = 0 \qquad \text{for } k - m = \text{odd} \tag{6}$$

The solution of the above equation determines the n_k values. Thus, $N_i(\lambda, \theta)$ in Eq. (4) can be written using the new Legendre functions:

$$N_i(\lambda_c, \theta_c) = \sum_{k=0}^{k_{max}} \sum_{m=0}^{k} [a_n^m \cos(m\lambda_c) + b_n^m \sin(m\lambda_c)]\, P_{n_k}^m(cos\theta_c) \tag{7}$$

Where k_{max} is the maximum degree yielding the nearest approximation of the specified function, λ_c and θ_c are longitudes and colatitudes in the spherical cap coordinate system (Al-Fanek, 2013). The new Legendre functions $P_{n_k}^m(cos\theta_c)$ in Eq. (7) are of order m and the non-integer degree n and its detailed computation can be found in (Al-Fanek, 2013). Therefore, Eq. (3) can be rearranged as:

$$\mathbf{Y} = \mathbf{A}(\mathbf{A}'\mathbf{x}) \tag{8}$$

Where $\mathbf{A}'$ is a matrix that contains the spherical cap harmonic basis functions. The matrix $\mathbf{x}$ contains the expansion coefficients that is equals to $(k_{max} + 1)^2$.

2.3. Empirical Orthogonal Function (EOF)

The empirical orthogonal functions (EOFs) are data driven orthogonal basis function that represent the maximum variance of a data set (Forootan, 2014). The EOFs in this study are obtained from the ERA5's humidity and temperature data on 37 pressure levels. This model's data have 1-hour temporal resolution and about 31-kilometer spatial resolution. Using the ERA5 data, wet refractivity can be calculated as:

$$es = a * e^{(\frac{b*t}{t+c})} \tag{9}$$

$$e = \frac{H * es}{100} \tag{10}$$

$$N_w = 3.732 * 10^5 * \frac{e}{T^2} \tag{11}$$

Where es represents the saturation vapor pressure in hpa, t is temperature in Celsius, H is relative humidity and T is temperature in Kelvin. The constant coefficients are $a = 6.1121$, $b = 17.502$ and $c = 240.97$, which are taken from (Recommendation, 2001). It is worth mentioning here that the latency of ERA5 is about 5 days. Thus, for real-time tomography applications, this model cannot be used. In such cases, alternative model outputs, such as in-house WRF[1] model runs, might replace those of ERA5. To compute the EOFs, the wet refractivity index profiles matrix are arranged as:

$$N_w = \begin{bmatrix} N(\lambda_{c1}, \varphi_{c1}, h_1, t_1) & \cdots & N(\lambda_{c1}, \varphi_{c1}, h_1, t_n) \\ \vdots & \ddots & \vdots \\ N(\lambda_{ck}, \varphi_{ck}, h_k, t_1) & \cdots & N(\lambda_{ck}, \varphi_{ck}, h_k, t_n) \end{bmatrix} \tag{12}$$

Where λ_{ci} and φ_{cj} represents are longitudes and colatitudes in the spherical cap coordinate system for k[th] voxel, h_k indicate altitude for the corresponding voxel, and t_n represents the considered time. In this matrix, rows and columns indicate spatial and temporal changes of the wet refractivity indices, respectively. The eigenvectors of the matrix N_w are the EOFs (Adavi and Mashhadi-Hossainali, 2015). The EOFs that correspond to bigger eigenvalues represent dominant role in describing the data's variance. The other EOFs that correspond to small eigenvalues are likely associated to noise (Bjornsson and Venegas, 1997). The vertical basis function using EOF's can be written as follows:

$$\mathrm{F} = \sum_{\mathrm{j}=1}^{\mathrm{p}} \alpha_{\mathrm{j}} (\mathrm{EOF})_{\mathrm{j}} = \sum_{\mathrm{j}=1}^{\mathrm{p}} \mathrm{Z}_{\mathrm{j}} \tag{13}$$

Where α_j are vertical basis function coefficients and p is the maximum number of EOF's. Combining SCH and EOF's, the wet refractivity values can be expanded as:

$$N_i(\lambda_c, \theta_c, \mathrm{h}) = \sum_{q=1}^{Q} \sum_{k=0}^{k_{max}} \sum_{m=0}^{k} [a_n^m \cos(m\lambda_c) + b_n^m \sin(m\lambda_c)] P_{n_k}^m (cos\theta_c) Z_q(\lambda_c, \theta_c, \mathrm{h}) \tag{14}$$

Here, h indicates the altitude of the corresponding voxel, $Z_q(\lambda_c, \theta_c, \mathrm{h})$ represent the EOFs, and $q = 1{:}\,Q$ represents their order. Thus, the number of unknown coefficients to determine N is $\mathrm{Q} \times (k_{max} + 1)^2$. In this study, the EOFs are obtained from the ERA5 model in a two-hour period before the tomography epoch. Fig. 1 displays the first 2 EOF derived from ERA5 data and their corresponding singular values. Fig. 1b indicates that the first EOF (EOF1) forms about 98% of the variance and the second EOF (EOF2) contains about 1% of variance. These two components are used to model the water vapor in the next section.

[1] https://www.mmm.ucar.edu/weather-research-and-forecasting-model

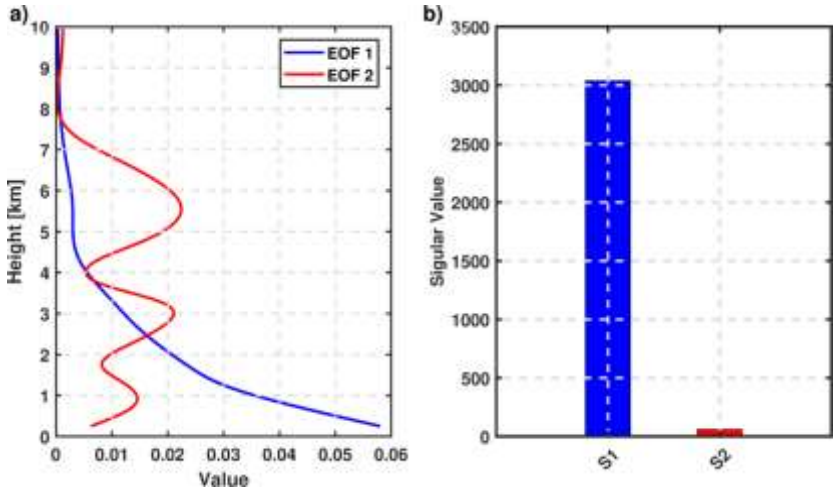

Fig. 1. An example of empirical orthogonal functions (EOFs) from ERA 5 data on 4th July 2018 over Germany. In a) The two profiles indicate the first two dominant EOFs, and in b) the corresponding singular values are shown.

The spectral or spatial resolution of SHCs and number of EOFs can be specified according to the coverage and strength of the signal and noise in measurements. But, using any base function technique introduces smoothing features in the estimated solution due to its simpler modelled representation. If the actual atmosphere state does not follow the variations described by these models, the changes in the strength of the events will be reflected by the measurements and the model coefficients will be estimated to minimize the residuals. From the used base functions, only EOFs are estimated empirically and as mentioned, the EOFs only introduce the general vertical variations, for which one parameter is estimated to control the amplitude and peak of the vertical curve.

2.4. B-Spline function for modelling temporal variability

The B-spline functions are used as in (Schmidt et al. , 2011) to represent a time-dependent variations. Any temporal signal, shown as $h(t)$, can be expanded using the polynomial B-splines as:

$$\mathrm{h(t)} = \sum_{\mathrm{k=0}}^{k_{j-1}} c_k^j \Phi_{\mathrm{k}}^{\mathrm{j}}(\mathrm{t}) \tag{15}$$

Where c_k^j are the unknown coefficients correlated in time, $\Phi_{\mathrm{k}}^{\mathrm{j}}$ are the normalized polynomial B-splines of order m, j is the B-spline surface resolution, and k_j is set of polynomial B-splines for selected surface resolution (Schmidt, Dettmering, 2011). In order to obtain a 4D model, coefficients of spherical cap harmonics can be written as follows:

$$c_{n,m}(t_q) = \sum_{k=0}^{k_{j-1}} c_{n,m,k}^j \Phi_k^j(t_q) \tag{16}$$

Eq. (16) can be expressed for all unknown coefficients as:

$$\mathbf{c_q} = \mathbf{C}\mathbf{u_q} \tag{17}$$

Where $\boldsymbol{C}$ contains the expansion of coefficients in time and $\mathbf{u_q}$ are the B-spline basis functions. Substituting Eq. (17) into Eq. (8) yields:

$$\mathbf{Y} = \mathbf{ACU} \tag{18}$$

Where $\mathbf{Y}$ is the observation matrix and $\mathbf{U} = [\mathbf{u_1}, \mathbf{u_2}, \dots, \mathbf{u_q}]$ indicates the expansion of B-spline basis functions (in time). To compute the unknowns in matrices $\mathbf{C}$, Eq. (18) should be rewritten using a tensor product approach as follows (Schmidt, Dettmering, 2011):

$$\mathrm{vec}\mathbf{Y} = (\mathbf{U^T} \otimes \mathbf{A})\mathrm{vec}\mathbf{C} \tag{19}$$

in which vec(.) is an operator that arranges the columns of matrices as a vector (Schmidt, Dettmering, 2011). While recognizing $\mathbf{X_1} = \mathbf{U^T} \otimes \mathbf{A}$ and defining $\boldsymbol{\beta_1} = \mathrm{vec}\mathbf{C}$ yields:

$$\widehat{\boldsymbol{\beta_1}} = (\mathbf{X_1}^\mathbf{T}\mathbf{P}\mathbf{X_1})^{-1}\mathbf{X_1}^\mathbf{T}\mathbf{P}\,\mathrm{vec}\mathbf{Y} \tag{20}$$

Where $\mathbf{P}$ is the weight matrix of the observations and can be weighted, e.g., with respect to the elevation of GPS satellites in the time of observation. The time-correlated unknown coefficients can be estimated by utilizing Eq. (20). The level of ill-posed condition of Eq. (20) can be examined using condition number as follows (Hansen, 1998):

$$k = \frac{\sigma_{max}}{\sigma_{min}} \tag{21}$$

Where σ_{max} and σ_{min} are the largest and smallest singular values of matrix $\mathbf{X_1}$, respectively. When k becomes large the discrete Picard condition will not be satisfied and the least-squares solution is not reliable (Hansen, 1990). In this study, the Tikhonov regularization method (Tikhonov and Arsenin, 1977), as discussed in (Farzaneh and Forootan, 2018), is used to estimate the unknown coefficients of the functional model.

3. Region of study and observations

The study area is the network of GPS stations in Germany that covers region between [6.85, 13.3] degrees for latitudes, and [47.9, 54] degrees for longitude. Tomography time is also considered on 15 days in summer and also 15 days in winter of the year 2018, to evaluate the implemented tomography in different atmospheric conditions. Fig. 2 displays the gridded network and the distribution of GPS stations in the region of study for epochs of 13th January and 4th July. The number of existing GPS stations is about 194 on day 13th January and 185 on 4th July. The lowest altitude of the stations is about 48 meters, therefore the first level of atmosphere segmentation is considered at the zero altitude. Since the wet refractivity index is close to the zero for altitudes higher than 10 km, the maximum height for the wet refractivity index estimation in the atmosphere can be assumed at about 10 km (Bender, Dick, 2011). Therefore, maximum height studied is 10 km, and the vertical resolution of voxels is set to be 500 meters. The area of the region under study is 720 km × 675 km and the horizontal distribution of the voxels is considered 45 km. Therefore, based on the network gridding choices, there are 4800 voxels in the region of study. To evaluate the accuracy of the

implemented tomography, the obtained wet refractivity profiles will be compared with the 8 existing radiosonde stations in the region. The radiosonde profiles have been obtained from University of Wyoming archive (http://weather.uwyo.edu). Survo et al. (Survo et al. , 2015) compared radiosonde Integrated Precipitable Water(IPW) column measurements with GPS and microwave radiometer instrument observations and showed that all agreed within 1 millimeter. Also in this study, the comparison of Cryogenic Frostpoint Hygrometer and Vaisala Radiosonde resulted in differences of mean humidity about 1%. The distribution of radiosonde stations in the region can be seen in Fig. 2. Also, radiosonde stations coordinate have been listed in table 1.

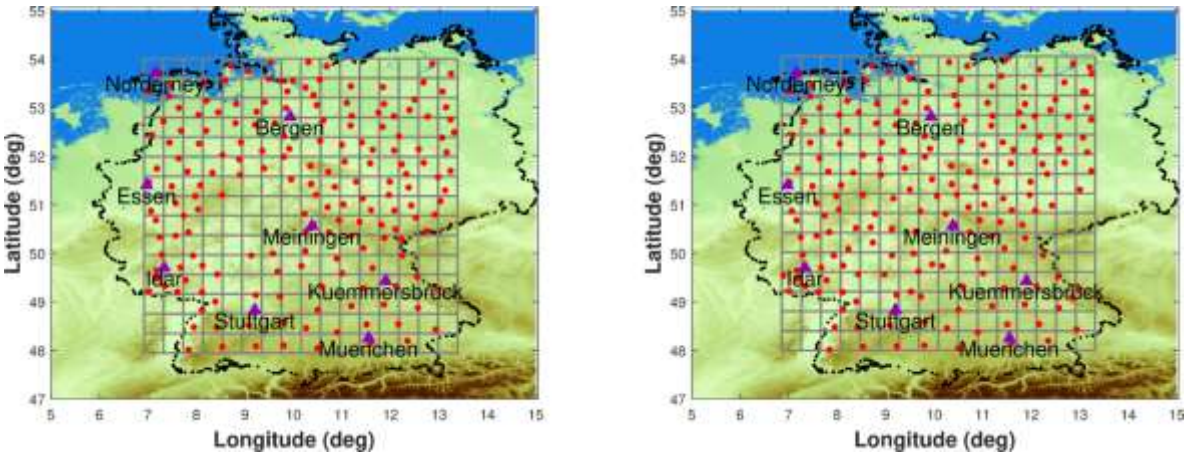

Fig. 2. The gridded network area including Germany. The red circles show GPS stations and the purple triangles represent radiosonde stations in the region. In a) we represent the distribution of GPS stations on January 13th, 2018, and in b) the distribution on July 4th, 2018.

Table 1. Radiosonde stations coordinate

Station name	Longitude(deg)	Latitude(deg)	Altitude(m)
Stuttgart	48.83	9.20	321
Idar	49.70	7.33	377
Meiningen	50.56	10.38	450
Essen	51.40	6.97	147
Bergen	52.81	9.93	69
Norderney	53.71	7.15	11
Muenchen	48.25	11.55	492
Kuemmersbruck	49.43	11.90	418

The values of the wet tropospheric delay at 30 second intervals estimated from the GPS network are used as input to the tomography approach. The IGS (International GNSS Service) final orbits are used in the solution, and the IGS final products are also considered for the interpolation of the satellites at 30-second time intervals, which is necessary for computing the signal length at different voxels. Here, we only use the data of Global Positioning System (GPS) constellation to treat all the receivers in the same manner. The cut

of angle of 15 degrees is chosen to eliminate erroneous observations. The GPT (Global Pressure and Temperature) model is used to calculate the initial value of dry tropospheric delay, and the VMF1 (Vienna Mapping Function) model is applied as mapping function for projecting the wet and dry tropospheric delays. The temporal resolution of the tomography is considered to be one-hour and is set in a way that the unknowns fall on the last epoch of each one-hour interval. The estimated unknowns and the radiosonde data are compared by computing Root Mean Squares of Errors (RMSEs), and statistical biases as (Xia, Cai, 2013):

$$RMSE = \sqrt{\frac{1}{n}\sum_{i=1}^{n}(N_{wm}^{i} - N_{w0}^{i})^2} \tag{22}$$

$$bias = \frac{1}{n}\sum_{i=1}^{n}(N_{wm}^{i} - N_{w0}^{i}) \tag{23}$$

where n is the number of unknowns in the retrieved profile, N_{wm}^{i} is the wet refractivity values estimated from the tomography solution in voxel i and N_{w0}^{i} is the wet refractivity values from the corresponding radiosonde data. The Pearson product-moment correlation coefficient (PCC as in Eq. (24)) (Lee Rodgers and Nicewander, 1988) is used for measuring the similarity of estimated profiles with those of radiosonde data as:

$$PCC = \frac{\sum_{i=1}^{n}(N_{wm}^{i} - \overline{N_w})\,(N_{w0}^{i} - \overline{N_{w0}})}{\sqrt{\sum_{i=1}^{n}(N_{wm}^{i} - \overline{N_w})^2}\,\sqrt{\sum_{i=1}^{n}(N_{w0}^{i} - \overline{N_{w0}})^2}} \tag{24}$$

In this equation $\bar{.}$ indicates the temporal average of variables. For showing the lack of correlation more visible, the value of $\mathbf{1} - \boldsymbol{PCC}$ has been calculated.

4. Results and discussions

4.1 Modelling 3D and 4D wet refractivity indices

The mathematical models for the 3D and 4D wet refractivity indices modelling are developed in 12 UTC and 24 UTC during 15 days in summer between 13 January and 2 February and also 15 days in winter between 4 July and 18 July of year 2018. Considered days in winter are not consecutive due to the lack of GPS stations in the network. Also in considered tomography epochs, for station Stuttgart in times 12 and 24 UTC of 5 July and station Bergen on time 24 UTC 7 July, radiosonde data was not available. Considering Eq. (14) and (15), the SCH degree (k_{max}), the maximum number of EOFs (Q), the order of B-splines (m), and resolution of B-splines (j) needs to be fixed. This is determined empirically by model (Al-Fanek, 2013), a function model will be developed for considered groups of parameters and the wet refractivity will be estimated. By comparing the tomography derived wet refractivity profiles with radiosonde measurements, the group of parameters that have the minimum mean RMSE will be selected as functional model parameters. For defining the resolution of functional model, the RMSE values of six radiosonde stations are considered and two stations are left out for independent comparisons. As mentioned in Section 2.3, the first EOF can recover about 98% of the wet refractivity behavior so the number of EOFs is considered equal to one (Q=1). To determine the remaining parameters, SCH degree considered between [2,

5], and B-spline level and resolution considered between [1, 5] and [0, 5] respectively. Then the functional model has been developed in the four tomography times for different groups of parameters. For example, in epochs of 12 UTC and 24 UTC on January 13th, 2018 and on July 4th, 2018, the average value of RMSE for considered model parameters in radiosonde stations can be seen in Fig. 3

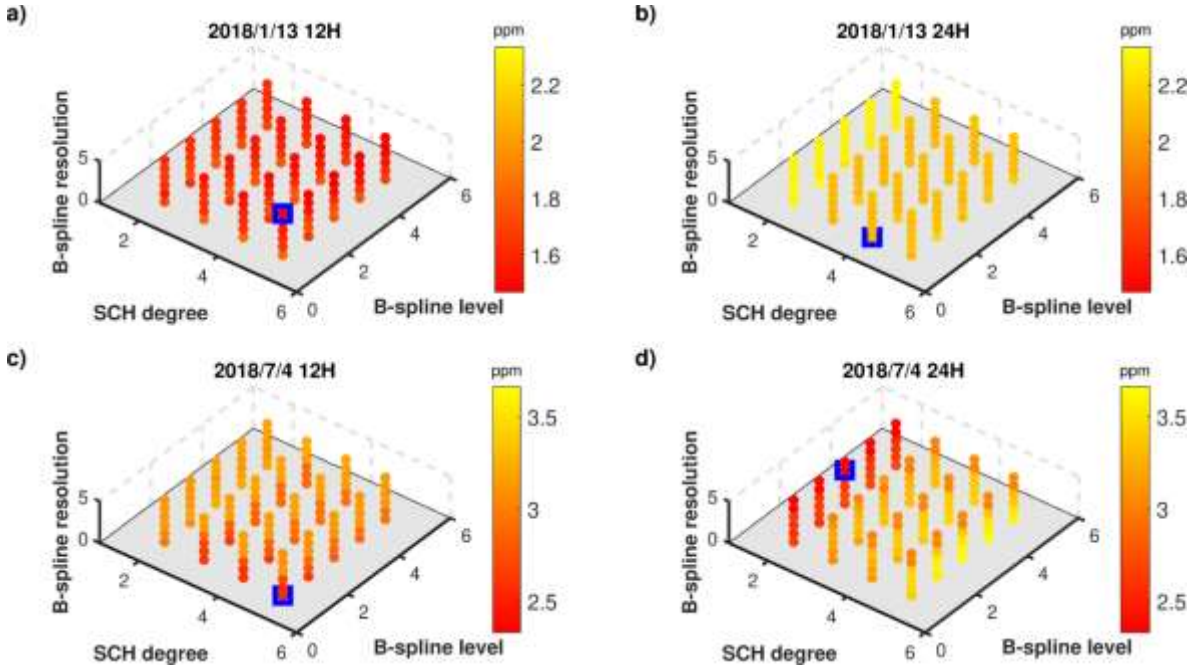

Fig. 3. Mean RMSE value of the 4D model parameters at the location of radiosonde stations for k_{max} between [2, 5], order of B-Spline between [1, 5], and resolution of B-spline [0, 5] in epochs of 12 UTC and 24 UTC on January 13th, 2018 and on July 4th, 2018. The x-axis of each diagram shows the different SCH degrees, the y-axis shows the different levels of the B-spline function, and the z-axis displays the B-spline surface resolutions for different parameters. The group of parameters for which the lowest RMSE is obtained is shown with blue squares.

As can be seen in Fig. 3, the range of RMSE changes about 0.3 ppm for two epochs of January 13th, 2018 but this variation is about 1 ppm for two epochs of July 4th, 2018. The reason for this may be attributed to the higher amount of water vapor in the atmosphere on July 4th compared because vigorous changes of the wet refractive index in the summertime lead to more sensitivity to the estimated parameters of the functional model.

To show the advantage of the implemented functional models over the conventional methods of solving the Eq. (3), the condition number (Hansen, 1998), as well as the discrete Picard condition (Hansen, 1990) are examined for epoch of 24 UTC on July 4th, 2018. According to the considered horizontal and vertical resolution for the region of study, the number of unknown parameters is equal to 4800. From Eq. (14), the parameters of the 3D functional model are k_{max} and Q. So with respect to Fig. 3d, k_{max} and Q have been chosen equal to 2 and 1 respectively. Therefore, the number of unknown parameters for the 3D functional model is equal to 9 in this epoch. In Fig. 4, the discrete Picard condition for conventional tomography method and 3D functional model has been shown. In this figure the red line indicates the singular value of the design matrix (σ_i), the blue line shows Fourier coefficients ($|u_i^T b|$), and the green line shows the proportion of Fourier coefficients to singular values

($\frac{|u_i^T b|}{\sigma_i}$). In Fig. 4b it can be shown that Fourier coefficients decay faster to zero compared to the corresponding singular values so the discrete Picard condition is satisfied. But in Fig. 4a, the last singular values decay faster to zero compared to the corresponding Fourier coefficients. So it can be seen that by using function-based tomography the problem becomes more well-posed and the discrete Picard condition is satisfied.

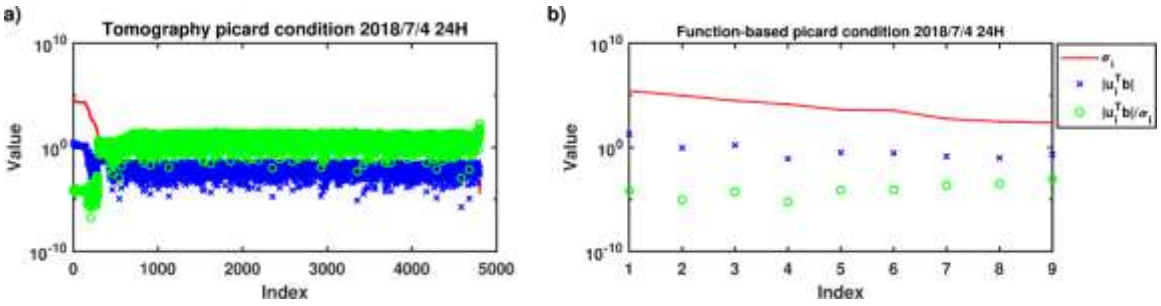

Fig. 4. Examining discrete Picard condition for a) conventional voxel-based tomography method and b) the 3D functional model of this study (Eq.(14)). Singular values of the design matrix (σ_i), corresponding Fourier coefficients ($|u_i^T b|$), and the proportion of Fourier coefficients to singular values ($\frac{|u_i^T b|}{\sigma_i}$) can be seen by the red line, blue stars, and the green circles, respectively.

4.2 Comparison of results with radiosonde profiles

According to the functional model parameters that have the minimum mean RMSE value, the wet refractivity can be estimated in the 3D (Eq. (14)) and 4D (Eq. (15)) models. In each 1 hours considered epochs, wet refractivity profiles derived from tomographic results have been compared to the corresponding radiosonde values as well as the calculated wet refractivity profiles from the ERA5 model. For example, Fig. 5 shows the differences between the 3D, 4D, and ERA5 vertical profiles with radiosonde measurements, in epochs of 12 UTC and 24 UTC on January 13th, 2018 and on July 4th, 2018. For all considered epochs, the 3D and 4D functional models have been developed and compared with radiosonde observations and ERA5 data, where the corresponding statistics at each tomography epoch are shown in Fig. 6. In all considered tomography epochs, the mean RMSE in different altitudes are calculated and can be seen in Fig. 7.

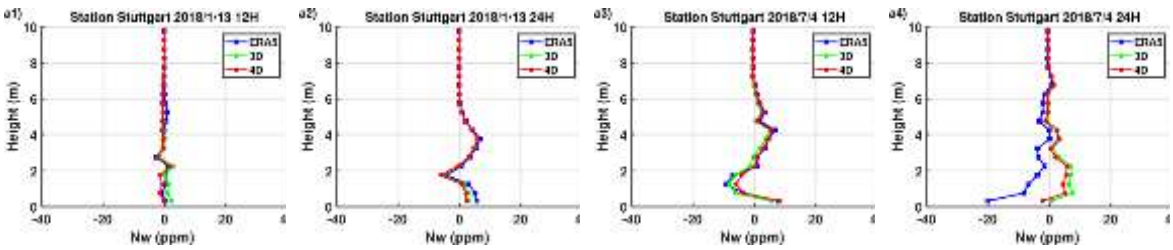

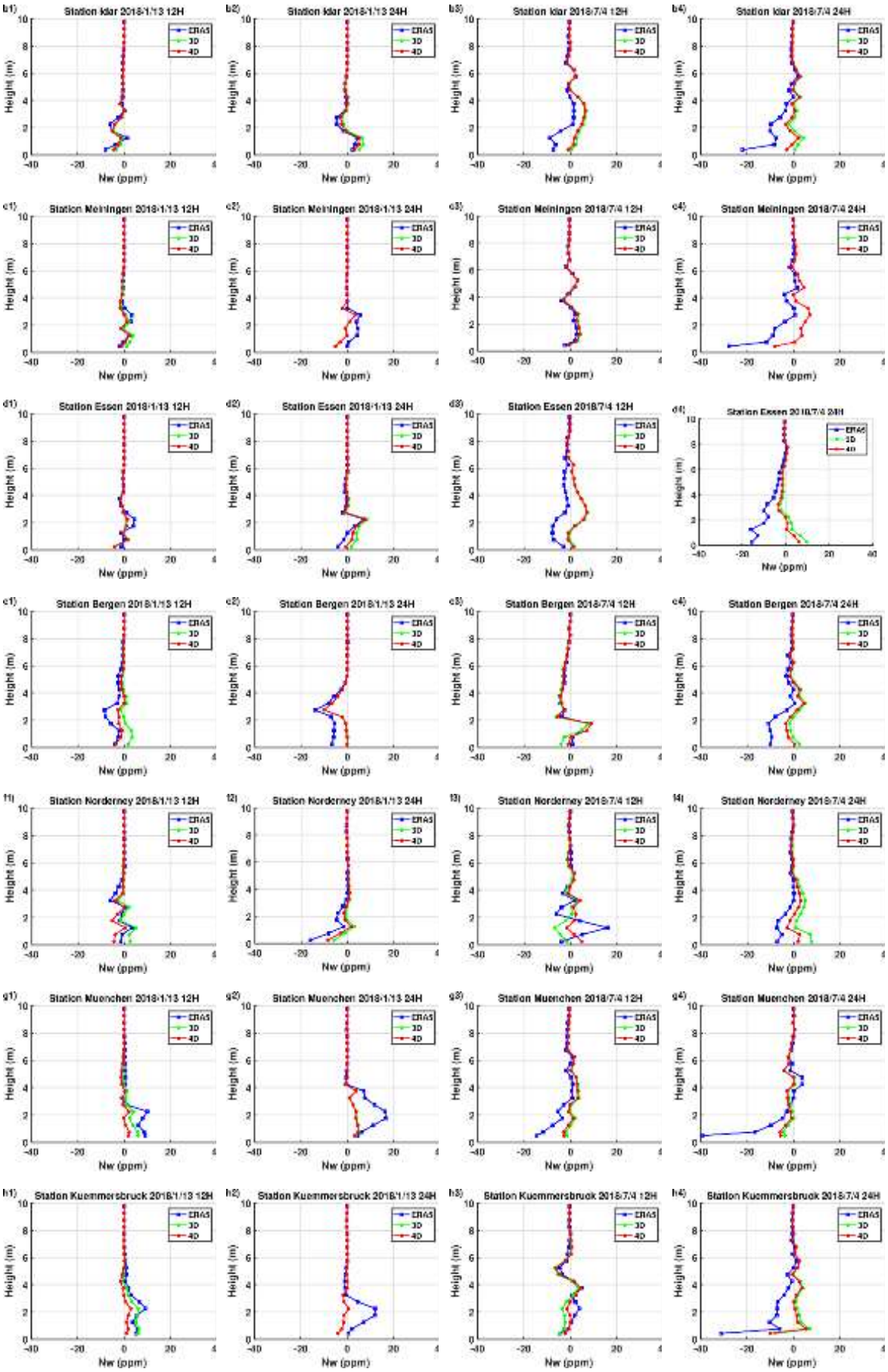
b1) Station Idar 2018/1/13 12H
b2) Station Idar 2018/1/13 24H
b3) Station Idar 2018/7/4 12H
b4) Station Idar 2018/7/4 24H
c1) Station Meiningen 2018/1/13 12H
c2) Station Meiningen 2018/1/13 24H
c3) Station Meiningen 2018/7/4 12H
c4) Station Meiningen 2018/7/4 24H
d1) Station Essen 2018/1/13 12H
d2) Station Essen 2018/1/13 24H
d3) Station Essen 2018/7/4 12H
d4) Station Essen 2018/7/4 24H
e1) Station Bergen 2018/1/13 12H
e2) Station Bergen 2018/1/13 24H
e3) Station Bergen 2018/7/4 12H
e4) Station Bergen 2018/7/4 24H
f1) Station Norderney 2018/1/13 12H
f2) Station Norderney 2018/1/13 24H
f3) Station Norderney 2018/7/4 12H
f4) Station Norderney 2018/7/4 24H
g1) Station Muenchen 2018/1/13 12H
g2) Station Muenchen 2018/1/13 24H
g3) Station Muenchen 2018/7/4 12H
g4) Station Muenchen 2018/7/4 24H
h1) Station Kuemmersbruck 2018/1/13 12H
h2) Station Kuemmersbruck 2018/1/13 24H
h3) Station Kuemmersbruck 2018/7/4 12H
h4) Station Kuemmersbruck 2018/7/4 24H
ERA5
3D
4D
Height (m)
Nw (ppm)

Fig. 5. Differences between the radiosonde data and the 3D-, 4D-tomography, and the ERA5-derived wet refractivity in epochs of 12 UTC and 24 UTC on January 13th, 2018 and on July 4th, 2018. The blue line indicates the difference of the ERA5 profile with radiosonde data, the red line shows the difference of the 4D model wet refractivity profiles with radiosonde data, the green line shows the difference of the 3D model profiles with radiosonde data at different altitudes. Locations of the radiosonde stations can be seen in Fig. 2.

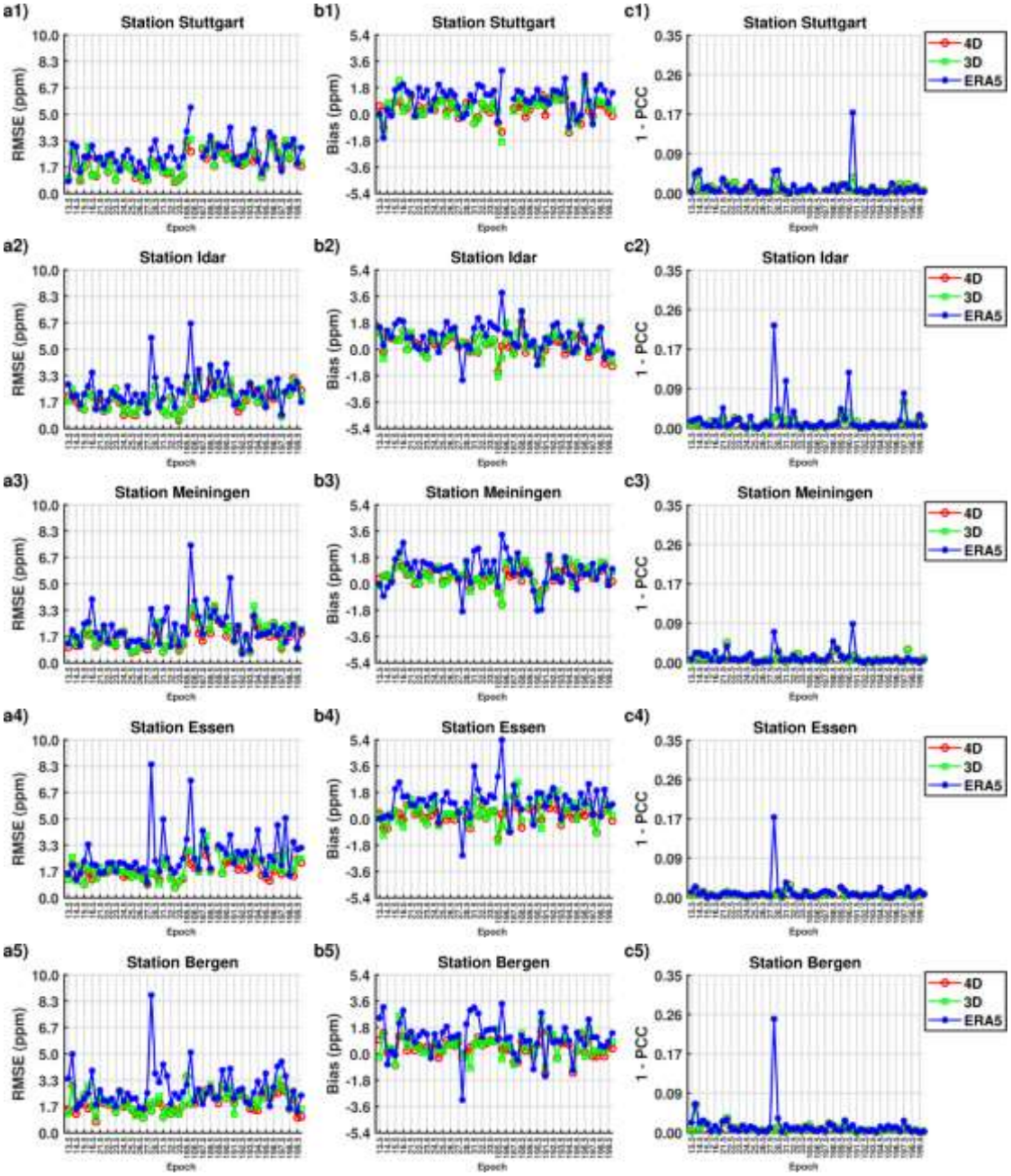

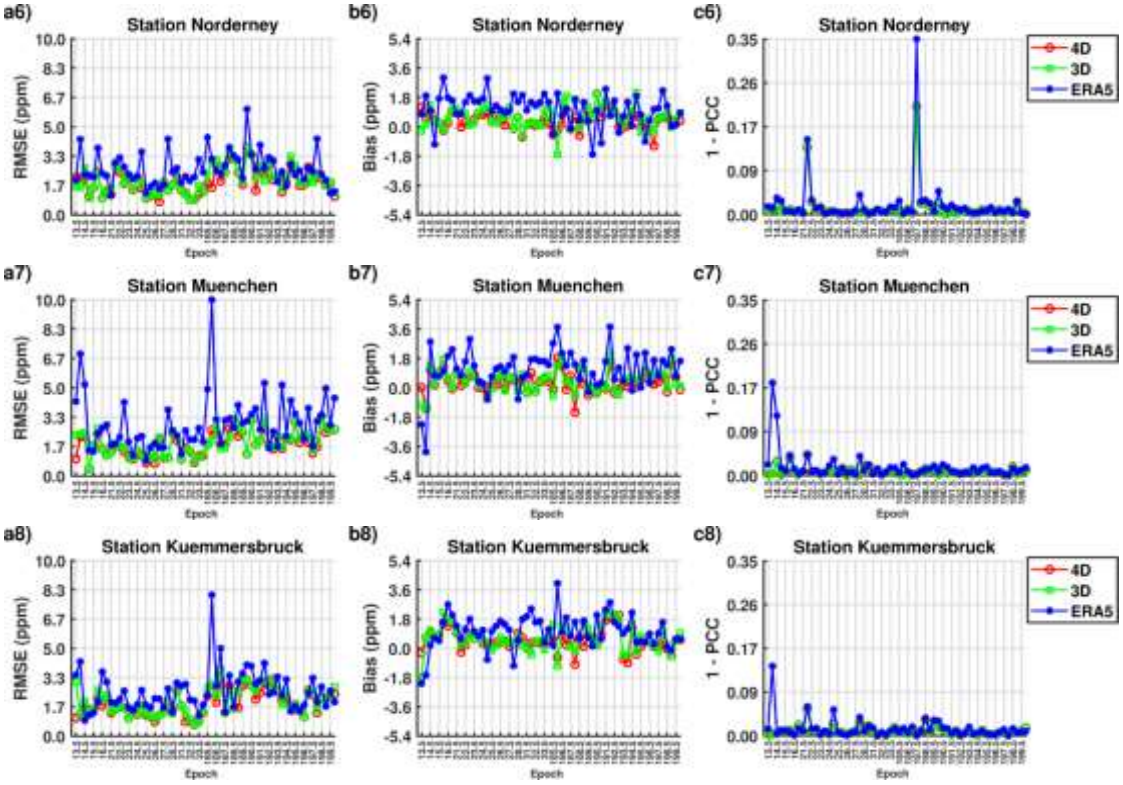

Fig. 6. The values of RMSE, bias, and 1-PCC at each tomography epoch. Red line correspond to the 4D model statistic parameters, green line show statistic parameters of the 3D models and blue line represent statistic parameters of the ERA5 data.

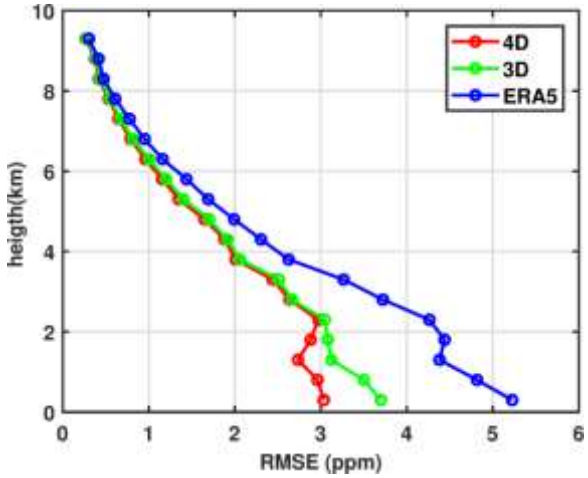

Fig. 7. Mean RMSE at different altitudes for the 4D, 3D, and ERA5 data in red, green, and blue lines respectively.

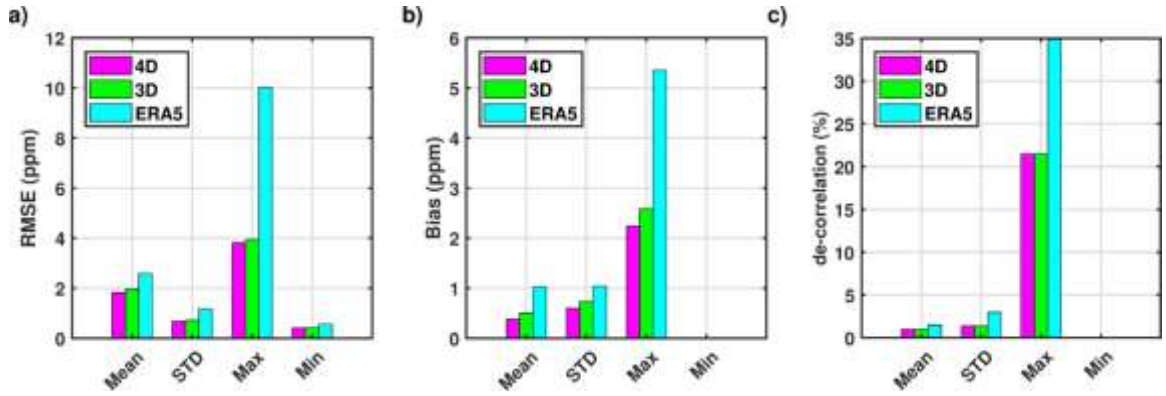

Fig. 8. Statistic Parameters for the RMSE, Bias, and 1-PCC value in all considered tomography epochs for 4D models, 3D models , and ERA5 data in magenta, green , and cyan charts respectively.

For all considered epoch and stations in the Fig. 6, Statistic parameters such as Mean, Standard deviation(STD), Maximum, and Minimum for the 4D model, 3D model, and ERA5 data for RMSE, Bias, and 1-PCC values have been calculated and displayed in Fig. 8. Also, in considered tomography epochs, the average percentage of improvement in RMSE value of the 3D and 4D model has been calculated with respect to RMSE of ERA5 profiles as well as the percentage of improvement in RMSE of the 4D model has been calculated with respect to RMSE of the 3D model. Mean Improvement percentages can be seen in Fig. 9.

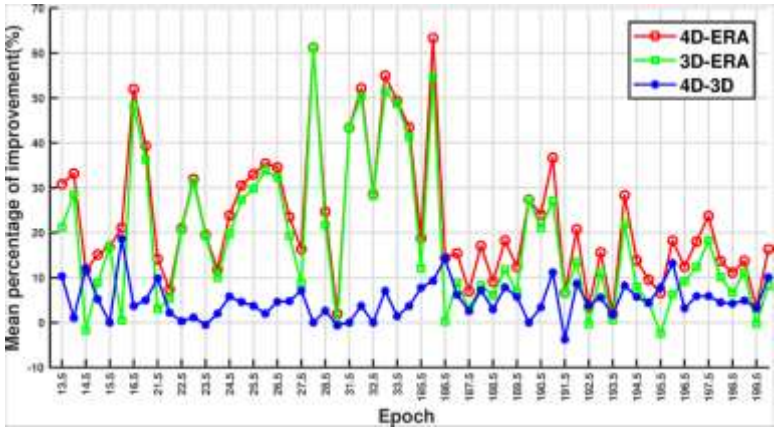

Fig. 9. The percentage of improvement of the 4D model versus ERA5 model, 3D model versus ERA5 model, and 4D model versus 3D model in the red, green, and blue bars, respectively. The mean improvement percentages are shown by the corresponding coloured lines.

According to Fig. 6c1, c2, c3, c4, c5, c6, c7, and c8, the 3D and 4D models have the same correlation with respect to the radiosonde data. This can be explained by the usage of the same vertical basis functions (EOF) for both models. As can be seen in Fig. 6 and Fig. 8, the implemented functional tomography has lower RMSE and Bias and 1-PCC Value compared to the ERA5 data with respect to the 8 radiosonde stations data, and also these parameters are lower for the 4D model compared to the 3D model. From Fig. 9, it can be concluded that 4D model and 3D model improve ERA5 RMSE value by average of 22 and 17 percent respectively and in some tomography epochs functional tomography models shows

improvement more than 50 percent in ERA5 data RMSE. Fig. 9 also shows that 4D model improves RMSE value by average of about 5 percent compared to the 3D model.

According to Fig. 8, the functional model tomography retrieved the wet refractivity indices profiles with mean values of RMSE, Bias, and 1-PCC of about 1.9 ppm, 0.45 ppm, and 1 percent respectively. Also from Fig. 8, it can be seen that implemented functional model has improved the Maximum Mean RMSE, Mean Bias, and Mean 1-PCC value up to 40 percent compared to ERA5 data. Fig. 8 also shows that in all considered epochs the 4D model has a positive percentage of improvement with respect to the ERA5 RMSE and the highest percentage of improvement for the 4D model is about 65 percent. As can be seen in Fig. 7, the 4D model has the lowest mean RMSE in altitudes below 3 km. This can be explained by the fact that the lowest altitudes have the most concentration and variation of wet refractivity index. So developing a time-dependent model decreased the RMSE value in these altitudes.

4.3 Zenith Wet Delay maps

After estimation of wet refractivity indices, Zenith Wet Delay (ZWD) for all tomography epochs can be calculated using Eq. (2) . Here for example ZWD maps in epochs of 12 UTC and 24 UTC on January 13th, 2018, and on July 4th, 2018 have been compared. For this purpose ZWD maps in the region of study for 3D, 4D, and ERA5 model as well as, the difference between represented functional models and ERA5 model can be seen in Fig. 10. For comparison of ZWD maps between functional model and ERA5 data, mean bias and PCC has been calculation for each ZWD map with respect to ERA5 calculated ZWD maps, and can be seen in Fig. 11.

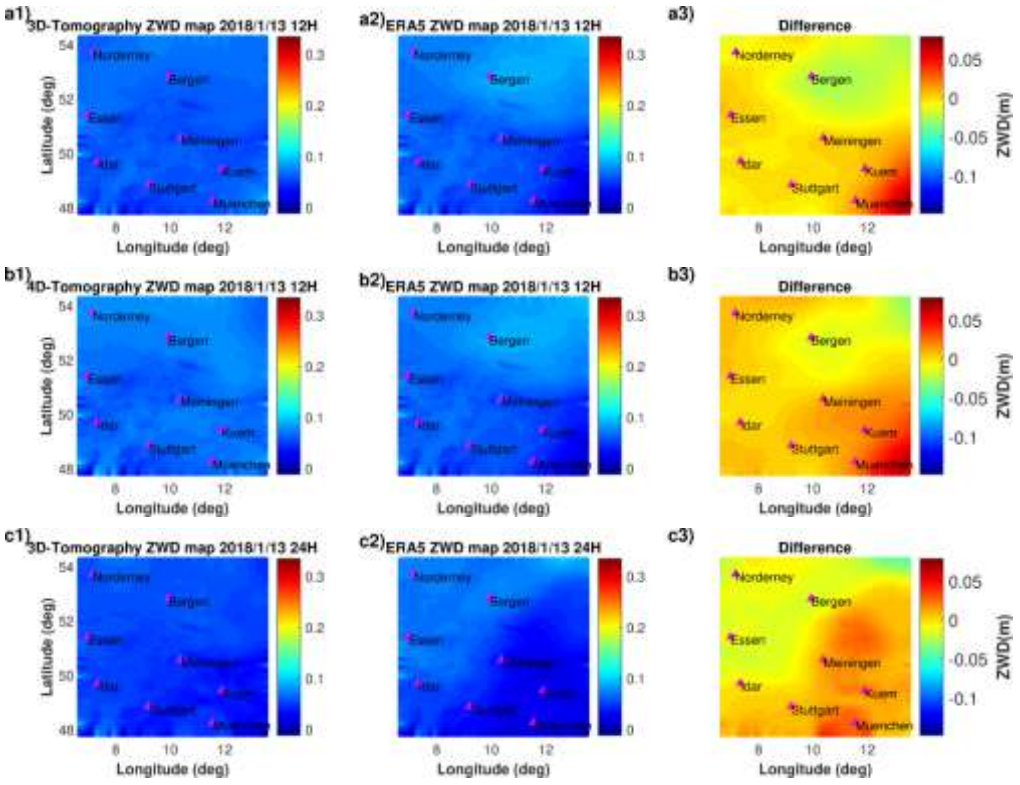

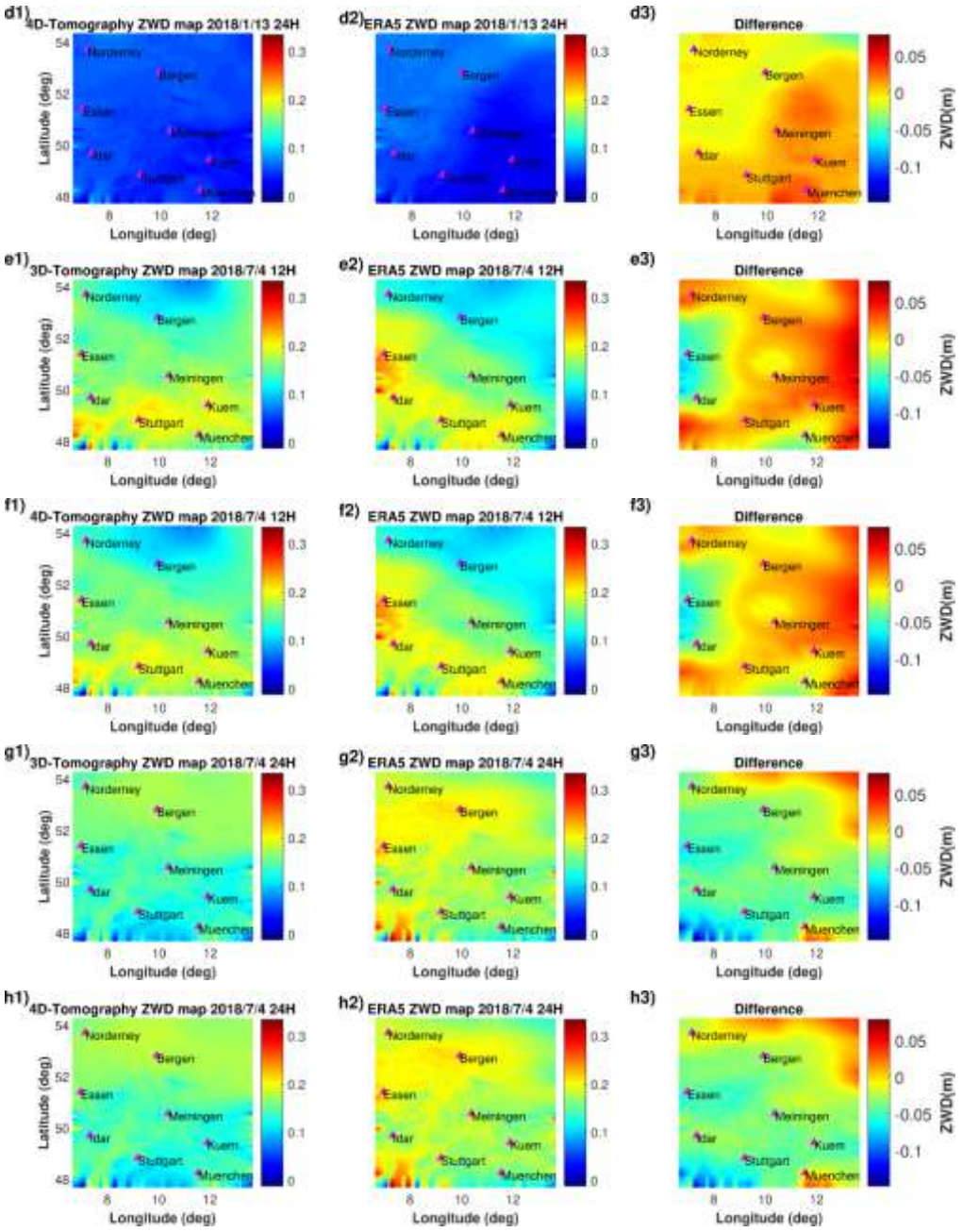

1 **Fig. 10.** Estimated Zenith Wet Delay for functional-based tomography models and a comparison of
2 those with ERA5 data. Radiosonde stations are presented with magenta triangles.

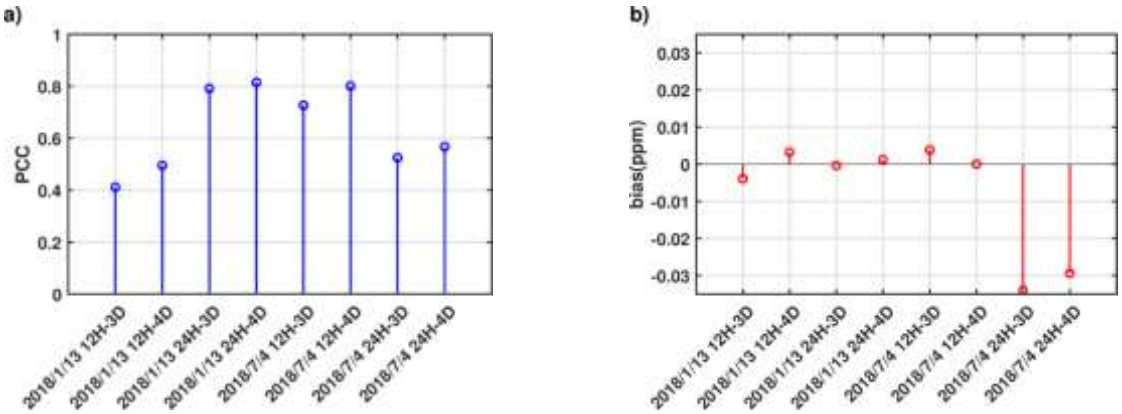

3 **Fig. 11**. Bias and PCC parameters calculated from ZWD maps for each considered method.

According to Fig. 10g2 and h2, at 24 UTC on 4th July 2018, the ERA5 data has the highest ZWD value among four considered epochs. Also, as can be seen in Fig. 6a7, b7, a8, and b8, that in this epoch ERA5 data have high RMSE and Bias Value for Muenchen and Kuemmersbruck stations. But according to Fig. 6c7, and c8, the Value of 1-PCC does not differ from functional models value. So for ERA5 data being bias resulted in the highest mean RMSE value in this epoch.

According to PCC values in Fig. 11a, the mean PCC value between functional models and ERA5 data is about 0.64. So it can be said that despite using ERA5 data for the construction of functional models, final tomography results are not completely correlated with ERA5 data due to effect of the GPS observations.

5. Conclusions and further research

In this research, a functional tomography approach was developed to retrieve the atmospheric refractive index, where a combination of the spherical cap harmonic functional models and the empirical orthogonal functions were applied to represent the three spatial dimensions and the B-splines were used to account for changes in time. Comparisons with 8 radiosonde stations in the area of study and the ERA5 data are conducted to investigate the feasibility and performance of the introduced technique under various tropospheric situations. To do this, we tested the estimated wet refractivity profiles at hour 12 and 24 UTC, during 30 different days in summer and winter of 2018. The results of study indicate that the wet refractivity profiles are reasonably well comparable with the radiosonde derived profiles in all considered station with the range of mean RMSE and Bias of about 1.9 ppm and 0.45 ppm respectively. The mean RMSEs between the ERA5 and radiosondes are found to be 2.6 ppm, and therefore in some epochs, the functional tomography is about 65% smaller. The results also show that the highest miscorrelation ($1 - PCC$, where PCC is estimated in Eq. (24)) of the retrieved profiles from the introduced functional tomography is about 20%, compared to the radiosonde profiles, when that of ERA5 is about 35%.

Tropospheric tomography is known to be an ill-posed inverse problem. Numerous factors such as the number, quality, and distribution of observations, parameterization and computation strategy can affect the quality of solving this inverse problem. For example, if the number of stations is small in some areas or the measured signals have poor geometry, troposphere modeling based on GPS data only is problematic. In addition, GPS measurements are not always available at all elevation angles, which will weaken the vertical resolution relative to the horizontal resolution. As a consequence of these issues, there are limitations in the quality and resolution of tropospheric tomography solutions. To alleviate these limitations, a priori information such as data/model derived empirical orthogonal functions can be used to enhance the vertical distribution of wet refractivity. Also, inclusion of other data sources in the tomography process might help improving horizontal and vertical resolution. For example, satellite-based observations such as GPS RO atmospheric profiles that provide auxiliary information with good vertical coverage, can be used to boost the number of observations of the upper troposphere. The Galileo, GLONASS and Beidou are examples of other constellations that can improve the quantity of SWD data, increasing the data coverage for the proposed inversion.

References

Adavi, Z., Mashhadi-Hossainali, M. 4D tomographic reconstruction of the tropospheric wet refractivity using the concept of virtual reference station, case study: northwest of Iran. Meteorology and Atmospheric Physics 126, 193-205, 2014.

Adavi, Z., Mashhadi-Hossainali, M. 4D-tomographic reconstruction of water vapor using the hybrid regularization technique with application to the North West of Iran. Advances in Space Research 55, 1845-54, 2015.

Al-Fanek, O.J.S. Ionospheric imaging for Canadian polar regions. University of Calgary, 2013.

Alizadeh, M. Multi-Dimensional modeling of the ionospheric parameters, using space geodetic techniques. Techn. Univ. Wien, 2013.

Alshawaf, F., Balidakis, K., Dick, G., Heise, S., Wickert, J. Estimating trends in atmospheric water vapor and temperature time series over Germany. Atmospheric Measurement Techniques 10, 3117, 2017.

Aster, R., Borchers, B., Thurber, C. Parameter estimation and inverse problems: Elsevier Academic. Borchers, CH Thurber–Elsevier-Academic Press, New York, London, 2005.

Bender, M., Dick, G., Ge, M., et al. Development of a GNSS water vapour tomography system using algebraic reconstruction techniques. Advances in Space Research 47, 1704-20, 2011.

Bender, M., Dick, G., Heise, S., et al. GNSS Water Vapor Tomography. 2013.

Bender, M., Raabe, A. Preconditions to ground based GPS water vapour tomography. Annales geophysicae. pp. 1727-34, 2007.

Bevis, M., Businger, S., Herring, T.A., Rocken, C., Anthes, R.A., Ware, R.H. GPS meteorology: Remote sensing of atmospheric water vapor using the Global Positioning System. Journal of Geophysical Research: Atmospheres 97, 15787-801, 1992.

Bjornsson, H., Venegas, S. A manual for EOF and SVD analyses of climatic data. CCGCR Report 97, 112-34, 1997.

Bosy, J., Rohm, W., Borkowski, A., Kroszczynski, K., Figurski, M. Integration and verification of meteorological observations and NWP model data for the local GNSS tomography. Atmospheric Research 96, 522-30, 2010.

Carvalho, D., Rocha, A., Gómez-Gesteira, M., Santos, C.S. Comparison of reanalyzed, analyzed, satellite-retrieved and NWP modelled winds with buoy data along the Iberian Peninsula coast. Remote sensing of environment 152, 480-92, 2014.

Chen, B., Liu, Z. Voxel-optimized regional water vapor tomography and comparison with radiosonde and numerical weather model. Journal of geodesy 88, 691-703, 2014.

Ding, N., Zhang, S., Zhang, Q. New parameterized model for GPS water vapor tomography. Annales Geophysicae. Copernicus GmbH, pp. 311, 2017.

Dong, Z., Jin, S. 3-D water vapor tomography in Wuhan from GPS, BDS and GLONASS observations. Remote Sensing 10, 62, 2018.

Eggermont, P.P.B., Herman, G.T., Lent, A. Iterative algorithms for large partitioned linear systems, with applications to image reconstruction. Linear algebra and its applications 40, 37-67, 1981.

Farzaneh, S., Forootan, E. Reconstructing Regional Ionospheric Electron Density: A Combined Spherical Slepian Function and Empirical Orthogonal Function Approach. Surveys in Geophysics 39, 289-309, 2018.

Flores, A., Ruffini, G., Rius, A. 4D tropospheric tomography using GPS slant wet delays. Annales Geophysicae. Springer, pp. 223-34, 2000.

Forootan, E. Statistical signal decomposition techniques for analyzing time-variable satellite gravimetry data. Universitäts-und Landesbibliothek Bonn, 2014.

Guerova, G., Jones, J., Douša, J., et al. Review of the state of the art and future prospects of the ground-based GNSS meteorology in Europe. Atmospheric Measurement Techniques 9, 5385-406, 2016.
Haines, G. Spherical cap harmonic analysis. Journal of Geophysical Research: Solid Earth 90, 2583-91, 1985.
Hansen, P.C. The discrete Picard condition for discrete ill-posed problems. BIT Numerical Mathematics 30, 658-72, 1990.
Hansen, P.C. Rank-deficient and discrete ill-posed problems: numerical aspects of linear inversion. SIAM, 1998.
Hersbach, H., Bell, B., Berrisford, P., et al. The ERA5 global reanalysis. Quarterly Journal of the Royal Meteorological Society 146, 1999-2049, 2020.
Hirahara, K. Local GPS tropospheric tomography. Earth, planets and space 52, 935-9, 2000.
Hofmann-Wellenhof, B., Lichtenegger, H., Wasle, E. GNSS–global navigation satellite systems: GPS, GLONASS, Galileo, and more. Springer Science & Business Media, 2007.
Hu, Z., Mallorquí, J.J. An Accurate Method to Correct Atmospheric Phase Delay for InSAR with the ERA5 Global Atmospheric Model. Remote Sensing 11, 1969, 2019.
Lee Rodgers, J., Nicewander, W.A. Thirteen ways to look at the correlation coefficient. The American Statistician 42, 59-66, 1988.
Leontiev, A., Rostkier-Edelstein, D., Reuveni, Y. On the Potential of Improving WRF Model Forecasts by Assimilation of High-Resolution GPS-Derived Water-Vapor Maps Augmented with METEOSAT-11 Data. Remote Sensing 13, 96, 2021.
Li, X., Dick, G., Lu, C., et al. Multi-GNSS meteorology: real-time retrieving of atmospheric water vapor from BeiDou, Galileo, GLONASS, and GPS observations. IEEE Transactions on Geoscience and Remote Sensing 53, 6385-93, 2015.
Limberger, M. Ionosphere modeling from GPS radio occultations and complementary data based on B-splines. Technische Universität München, 2015.
Liu, J., Chen, R., An, J., Wang, Z., Hyyppa, J. Spherical cap harmonic analysis of the Arctic ionospheric TEC for one solar cycle. Journal of Geophysical Research: Space Physics 119, 601-19, 2014.
Liu, J., Chen, R., Wang, Z., Zhang, H. Spherical cap harmonic model for mapping and predicting regional TEC. GPS solutions 15, 109-19, 2011.
Liu, Z. Ionosphere tomographic modeling and applications using Global Positioning System (GPS) measurements. 2004.
Nilsson, T., Gradinarsky, L. Water vapor tomography using GPS phase observations: simulation results. IEEE Transactions on Geoscience and remote sensing 44, 2927-41, 2006.
Raymund, T., Pryse, S., Kersley, L., Heaton, J. Tomographic reconstruction of ionospheric electron density with European incoherent scatter radar verification. Radio Science 28, 811-7, 1993.
Razin, M.R.G., Voosoghi, B. Regional ionosphere modeling using spherical cap harmonics and empirical orthogonal functions over Iran. Acta Geodaetica et Geophysica 52, 19-33, 2017.
Recommendation, I. 453-9, The radio refractive index: its formula and refractivity data. Recommendations and Reports of the ITU-R 8, 618-7, 2001.
Schmidt, M., Dettmering, D., Mößmer, M., Wang, Y., Zhang, J. Comparison of spherical harmonic and B spline models for the vertical total electron content. Radio Science 46, 2011.
Stierman, E. Precipitable water vapour estimation using GPS in Uganda: Measuring and modelling the precipitable water vapour using single and dual frequency GPS receivers. 2017.
Subirana, J.S., Hernandez-Pajares, M., Zornoza, J.e.M.J. GNSS Data Processing: Fundamentals and Algorithms. European Space Agency, 2013.

Survo, P., Leblanc, T., Kivi, R., Jauhiainen, H., Lehtinen, R. Comparison of selected in-situ and remote sensing technologies for atmospheric humidity measurement. Proceedings of the 19th Conference on Integrated Observing and Assimilation Systems for the Atmosphere, Ocean and Land Surface, Phoenix, AZ. 2015.

Tikhonov, A.N., Arsenin, V.Y. Solutions of ill-posed problems. New York, 1-30, 1977.

Trampert, J., Leveque, J.J. Simultaneous iterative reconstruction technique: physical interpretation based on the generalized least squares solution. Journal of Geophysical Research: Solid Earth 95, 12553-9, 1990.

Wang, X., Wang, X., Dai, Z., et al. Tropospheric wet refractivity tomography based on the BeiDou satellite system. Advances in Atmospheric Sciences 31, 355-62, 2014.

Xia, P., Cai, C., Liu, Z. GNSS troposphere tomography based on two-step reconstructions using GPS observations and COSMIC profiles. Annales geophysicae. Copernicus GmbH (Copernicus Publications) on behalf of the European Geosciences Union (EGU), 2013.

Xiaoying, W., Ziqiang, D., Enhong, Z., Fuyang, K., Yunchang, C., Lianchun, S. Tropospheric wet refractivity tomography using multiplicative algebraic reconstruction technique. Advances in Space Research 53, 156-62, 2014.

Yang, H., He, C., Wang, Z., Shao, W. Reliability Analysis of European ERA5 Water Vapor Content Based on Ground-based GPS in China. 2019 International Conference on Wireless Communication, Network and Multimedia Engineering (WCNME 2019). Atlantis Press, 2019.